PAPER

Bias-dependent spectral tuning in InP nanowire-based photodetectors

To cite this article: Vishal Jain *et al* 2017 *Nanotechnology* **28** 114006

IOP Publishing Nanotechnology
Nanotechnology 28 (2017) 114006 (8pp) https://doi.org/10.1088/1361-6528/aa5236

Bias-dependent spectral tuning in InP nanowire-based photodetectors

Vishal Jain[1,2], Magnus Heurlin[1], Mohammad Karimi[1,2], Laiq Hussain[1,2], Mahtab Aghaeipour[1], Ali Nowzari[1], Alexander Berg[1], Gustav Nylund[1], Federico Capasso[3], Lars Samuelson[1], Magnus T Borgström[1] and Håkan Pettersson[1,2]

[1] Solid State Physics and NanoLund, Lund University, PO Box 118, SE-221 00 Lund, Sweden
[2] Laboratory of Mathematics, Physics and Electrical Engineering, Halmstad University, PO Box 823, SE-301 18 Halmstad, Sweden
[3] School of Engineering and Applied Sciences, Harvard University, Cambridge, MA 02138, United States of America

E-mail: hakan.pettersson@hh.se

Received 11 September 2016, revised 23 November 2016
Accepted for publication 7 December 2016
Published 17 February 2017

Abstract

Nanowire array ensembles contacted in a vertical geometry are extensively studied and considered strong candidates for next generations of industrial scale optoelectronics. Key challenges in this development deal with optimization of the doping profile of the nanowires and the interface between nanowires and transparent top contact. Here we report on photodetection characteristics associated with doping profile variations in InP nanowire array photodetectors. Bias-dependent tuning of the spectral shape of the responsivity is observed which is attributed to a Schottky-like contact at the nanowire–ITO interface. Angular dependent responsivity measurements, compared with simulated absorption spectra, support this conclusion. Furthermore, electrical simulations unravel the role of possible self-gating effects in the nanowires induced by the ITO/SiO_x wrap-gate geometry. Finally, we discuss possible reasons for the observed low saturation current at large forward biases.

Supplementary material for this article is available online

Keywords: nanowires, nanowire arrays, IR photodetectors, solar cells, nanophotonics

(Some figures may appear in colour only in the online journal)

1. Introduction

Over the last two decades there has been a dramatic increase in research activities related to nanowires (NWs) due to their exciting prospects for implementation in novel high-performance transistors [1], LEDs [2], lasers [3], photodetectors [4, 5] and sensors [6] compatible with main-stream silicon technology. The NW device geometry plays a crucial role in many photonic applications e.g. photodetectors and solar cells, in which a strong absorption can be obtained by proper tailoring of NW diameter, length and pitch [7–10]. Previously, we have shown that the length of the n^+- and i-segments is crucial for obtaining a high efficiency of 13.8% in p^+–i–n^+ InP NW solar cells [11]. We have also reported on the importance of including a sufficiently long p^+-segment to decouple the NWs from the substrate and to shift the spatial location of charge carrier generation and collection to the upper part of the NWs [12].

So far, most studies on NW-based solar cells and photodetectors have focused on the spectral response under short-circuit bias conditions, with little attention given to the bias-dependence. In addition, the influence of doping levels in the different segments of NW p^+–i–n^+ photodetectors and solar cells have not been extensively studied. In this work, we present a study of the influence of doping levels in the absorption segment and the top segment on the electrical and optical properties of InP NW photodetectors. We have also carried out extensive device modeling for further understanding of the experimental results.

2. Methods

A sample series was fabricated with 130 nm diameter InP NWs grown on p^+ InP substrates in which the doping concentration in the absorption segment and the top segment was varied (table S1 in the online supplementary data). In the following, we discuss details related to growth, processing, measurements and simulations.

2.1. Nanowire growth

Periodic patterns of circular holes with diameter of 180 nm and a 400 nm pitch yielding a density of 6.25 μm^{-2} were prepared by nanoimprint lithography on p^+-InP (111)B substrates (Zn-doped to $5 \times 10^{18}\,cm^{-3}$) [13]. Catalyst Au nanoparticles were defined on the patterned substrate by metal evaporation and lift-off of 20 nm Au films. Alternative commercially-viable techniques such as Au electrodeposition in nano-sized holes would result in similar results [14]. NWs were subsequently grown in a low-pressure (100 mbar) metal organic vapor phase epitaxy (MOVPE) system (Aixtron 200/4), with a total flow of $13\,l\,min^{-1}$ using hydrogen (H_2) as carrier gas. For InP growth, trimethylindium (TMI) and phosphine (PH_3) were used as precursors, while diethylzinc (DEZn) was used as p-dopant precursor [15] and tetraethyltin (TESn) as n-dopant precursor [16]. Hydrogen chloride (HCl) at a molar fraction of $\chi_{HCl} = 6.1 \times 10^{-5}$ was used to inhibit the radial growth [17]. Before growth, the samples were first annealed at 550 °C for 10 min under a PH_3/H_2 gas mixture to desorb any surface oxides at a constant molar fraction of $\chi_{PH3} = 6.9 \times 10^{-3}$. The reactor was then cooled to 440 °C, at which point growth was initiated by the addition of TMI and DEZn to the gas flow at molar fractions of $\chi_{TMI} = 7.4 \times 10^{-5}$ and $\chi_{DEZn} = 6.1 \times 10^{-5}$, respectively. After a 30 s nucleation time, HCl was introduced. The grown InP p^+-segment has a nominal acceptor concentration of about $5 \times 10^{18}\,cm^{-3}$ [15].

For sample A, TESn was used with a molar fraction of $\chi_{TESn} = 3.5 \times 10^{-8}$ for the n^--doping in the absorption segment and $\chi_{TESn} = 4.8 \times 10^{-6}$ for the n-doping in the top n-segment resulting in estimated doping concentrations of $5-10 \times 10^{15}\,cm^{-3}$ and $1-3 \times 10^{17}\,cm^{-3}$, respectively, based on previous studies [16, 18]. After completing the top n-segment, the growth was terminated and the sample was cooled down in a PH_3/H_2 gas mixture. The only difference in the growth parameters for sample B was a reduced TMI flow rate ($\chi_{TMI} = 5.2 \times 10^{-5}$) while growing the top n^+-segment, effectively increasing the Sn incorporation [19] to an estimated doping level higher than $5 \times 10^{18}\,cm^{-3}$. Sample C had similar top n^+-doping as sample B, whereas the absorption segment was unintentionally doped ($\sim 1 \times 10^{15}\,cm^{-3}$) [18]. The grown NWs had a diameter of 130 nm and a length of approximately 2 μm.

2.2. Device processing

The standard vertical processing of detector elements (800 $\mu m \times 800\,\mu m$ in size, 4 million NWs connected in parallel) was done by depositing 55 nm insulating SiO_x on the as-grown samples, subsequent etching of SiO_x and Au catalyst from the tip of the NWs followed by deposition of a 50 nm ITO layer (figures 1(a) and (b)), as described elsewhere [11, 20, 21]. To get a smooth surface for wire-bonding of the devices, needed for further electro-optical characterization, a method was developed for removing the NWs in the desired bonding pad area by wet-etching prior to SiO_x deposition. In this case, it was observed that the partially etched NWs on the edges of the devices could potentially lead to significant leakage (figure S1(a) in the online supplementary data). To overcome this, instead of wet-etching the NWs, a hard-baked photoresist with thickness larger than the NW length was used as a lifting layer on top of which the ITO layer, followed by the Ti/Au bonding pad layer, was deposited (schematic shown in figure S1(b) in the online supplementary data).

2.3. Measurements

The spectrally resolved photocurrent (PC) was measured using a Bruker Vertex 80 v Fourier transform spectrometer housing an integrated Janis PTSHI-950-FTIR pulse-tube closed-cycle cryostat. The spectrometer was evacuated to avoid any influence of absorption lines in air. The spectrometer was equipped with a CaF_2 beam splitter and a quartz lamp. The modulated (~7.5 kHz) PC was amplified using a Keithley 428 programmable current amplifier. The photon flux from the quartz lamp was measured using a calibrated NIST Si photodiode with known responsivity and subsequently used to normalize the measured PC data. The *I–V* characteristics were measured with a Keithley 6430 sub-femtoampere sourcemeter.

For electroluminescence (EL) measurements, a Keithley 2612B sourcemeter was used to inject current while the EL signal was collected using an objective lens, collimated by a mirror, diffracted by a grating and then focused and dispersed over a Si CCD to record the signal.

2.4. Simulations

The opto-electrical simulations were carried out using the semiconductor module of COMSOL Multiphysics. The optical part involved calculating the wavelength-dependent absorption spectra of InP NWs for both normal and oblique (45°) incidence [22]. The electrical simulations were based on the drift-diffusion model in which the carrier and current densities were obtained by solving the Poisson equation and the continuity equations. The reported values of the radiative recombination coefficient ($1.2 \times 10^{-10}\,cm^3\,s^{-1}$) [23], the non-radiative electron (2 ns) and hole (3 ns) lifetimes [24, 25] and the Auger recombination coefficient ($9 \times 10^{34}\,cm^6\,s^{-1}$ [26] were used. The geometry included the doping profile ($5 \times 10^{18}/5 \times 10^{15}/1 \times 10^{17}\,cm^{-3}$) in the p^+–n^-–n InP NWs and electrical properties of SiO_2 with standard materials parameters, e.g. carrier mobilities, relative permittivities, bandgaps and electron affinities [27]. The saturation in drift mobility at high electric-fields was calculated using reported

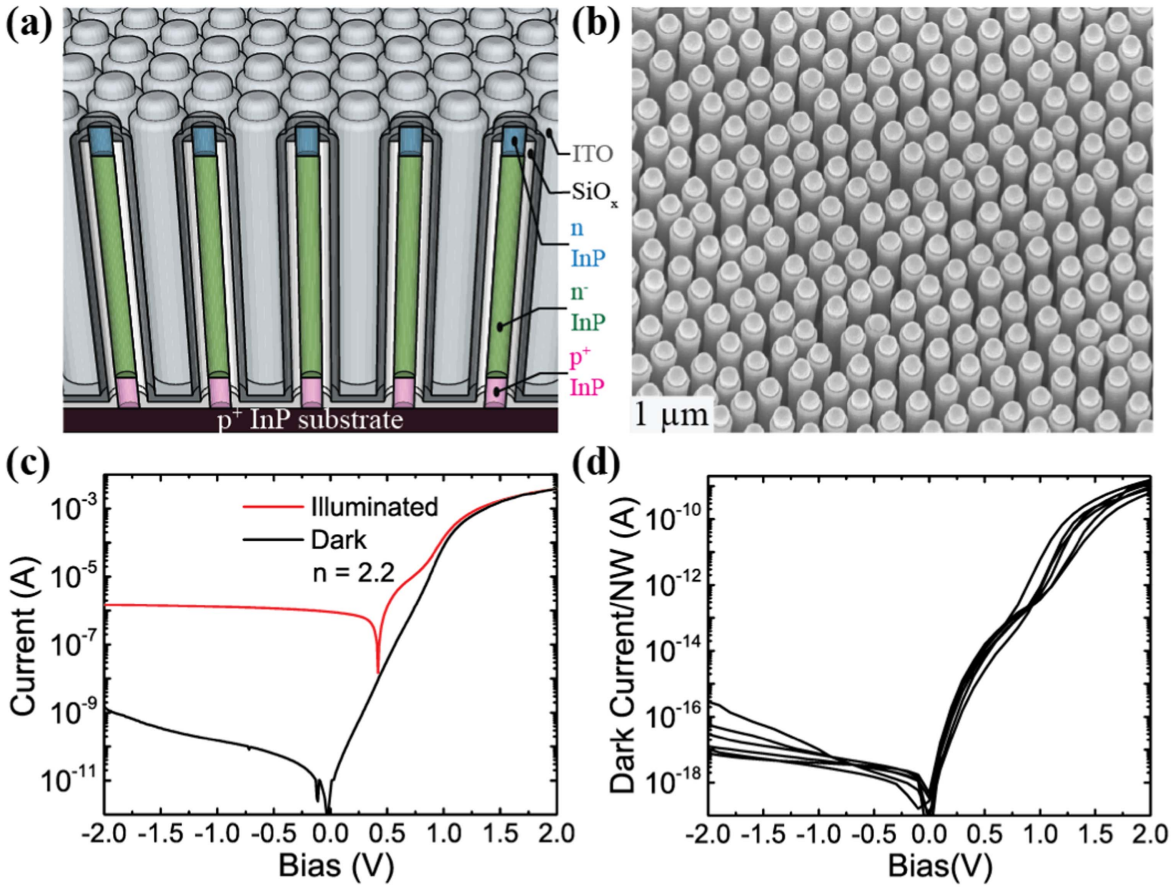

Figure 1. (a) Schematic of the array detectors (sample A). (b) SEM image of a fully processed device comprising 4 million NWs connected in parallel. (c) *I–V* characteristics in semi-log scale at 300 K with an ideality factor $n = 2.2$ extracted from the slope at forward bias. (d) Dark *I–V*/NW for six different devices at 300 K showing the small spread in *I–V* characteristics among different devices.

empirical formulas [28] in addition to the Caughey–Thomas mobility model [29].

3. Results and discussion

For sample A, comprising a p^+–n^-–n structure (see methods section for more details), the *I–V* characteristics typically showed an ideality factor of about 2.2 and an open-circuit voltage (V_{OC}) of 0.43 V at 300 K (figure 1(c)), comparable to the values obtained earlier for similar devices [12]. Differences in *I–V* characteristics were obtained when comparing devices (figure 1(d)). Such process-induced variations are expected since millions of NWs are contacted in parallel in these devices.

An expected monotonic decrease in responsivity is initially observed for decreasing reverse bias (figure S2 in the online supplementary data and figure 2(b)) and for increasing forward bias smaller than V_{OC} (figures 2(a) and (b)). The decrease in responsivity is due to the combination of a contraction of the axial space charge region towards the base of the NWs and a loss of high energy photons in the upper part of the NWs as discussed below and elsewhere [11, 12]. Interestingly, around a bias corresponding to V_{OC}, sample A exhibits a significant bias-dependent change in the spectral shape of the responsivity. In particular, the relative contribution of high-energy peaks (at about 2.0 and 2.3 eV) increases upon applying forward biases above V_{OC} (figures 2(a) and (b)), with a substantial change at 5 K (figure 2(b)). Moreover, *I–V* measurements under illumination show surprising results. The integrated (all-wavelengths) PC (insets of figures 2(a) and (b)), defined as the total current measured under illumination subtracted by the corresponding dark current, should have the same polarity independent of the bias. From the inset in figure 2(a), however, it can be seen that the PC changes sign from expected negative values, to positive values above V_{OC}. Similar results were obtained at 5 K with a pronounced broad high energy peak, emerging above V_{OC} (figure 2(b)). The straight-forward extraction of PC from the dark and illuminated DC sweeps was found to be in good agreement with AC lock-in chopper measurements (figure S3 in the online supplementary data).

The change in sign of the integrated PC indicates the presence of an additional junction connected back-to-back with the existing p–n junction within the NWs. This interesting result, actually pointing to possible applications in bias-tunable photodetectors, might be due to an unexpected difficulty to obtain low-ohmic contacts to the top n-segment of the NWs using Sn doping. Typically, the doping concentration in the top n-segment should be degenerate, i.e. higher than the effective conduction band density of states of

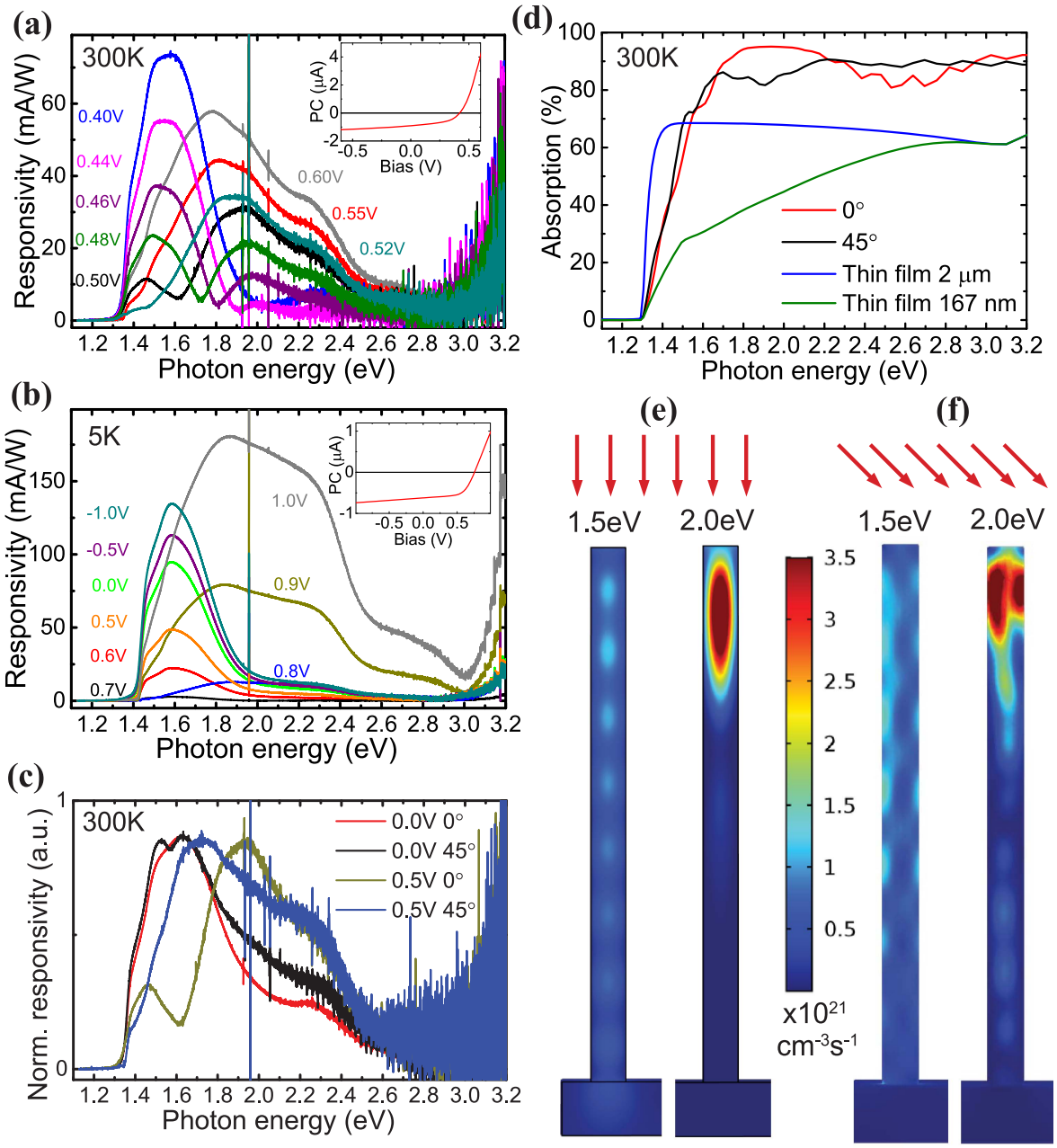

Figure 2. Bias-dependent responsivity of sample A measured at (a) 300 K and (b) 5 K. The sharp signal at 1.96 eV is due to the built-in red laser used in the Fourier transform spectrometer to keep track of the position of the scanning mirror. The insets show the bias dependence of the integrated photocurrent in linear scale. (c) Angle- and bias-dependence of the normalized responsivity for sample A. (d) Simulated absorption spectra of InP NW arrays at normal (red trace) and 45° tilted (black trace) incidence, along with comparative absorption spectra of a planar InP film with thickness of 2 μm (blue trace) and of 167 nm (green trace) corresponding to the same length and volume as the NWs, respectively. The absorbed photon density profiles for a unit cell with NWs under (e) normal and (f) 45° oblique incidence.

$5.7 \times 10^{17}\,\mathrm{cm}^{-3}$ at 300 K [27]. Such a doping level was difficult to achieve in the top n-segment of sample A due to the low doping level in the n^--segment and the limited range of the dopant source in the MOVPE. A low Sn doping level poses challenges for ohmic contact formation and could explain the presence of a Schottky-like contact between the NW top segment and the ITO contact layer. The high electric field in the near-surface depletion region related to this junction could under reverse bias conditions (i.e. for the case of the sample being forward-biased) effectively separate photo-induced charge carriers leading to a reversed PC, in particular at high photon energies where the absorption is expected to be higher in the top segment [11]. It should be mentioned here that measurements of planar sputtered ITO/n-InP junctions with doping concentrations of 2–4 $\times$ $10^{16}\,\mathrm{cm}^{-3}$ have previously indicated a negligible Schottky barrier [30, 31]. However, the exact interface conditions in the present case between NWs of only 130 nm diameter and sputtered ITO could differ significantly from those of planar interfaces.

These observations were further explored using angle-dependent responsivity measurements. The normalized

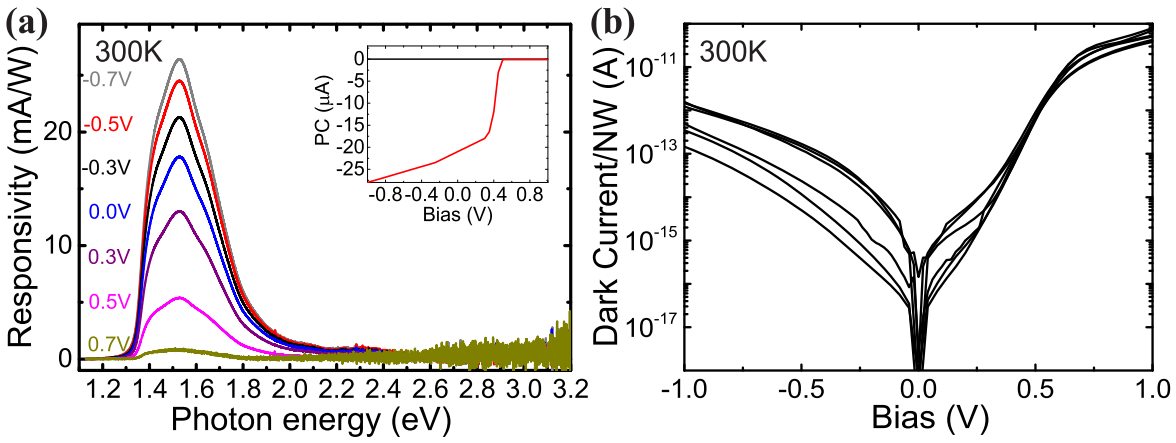

Figure 3. (a) Responsivity of sample B (p^+–n^-–n^+) for different biases measured at 300 K. The inset shows the photocurrent measured with chopper at 100 Hz using a lock-in amplifier. (b) Dark *I*–*V*/NW for six sample B devices at 300 K.

responsivity plots (figure 2(c)) reveal that the relative contribution of high-energy photons to the PC under short-circuit conditions increases with oblique incidence (45°) of the incoming light. Simulations of absorption characteristics (see section 2.4 for details) were invoked to provide insight into these responsivity measurements. The results first of all show enhanced absorption in the NW arrays, both at normal (0°) and oblique (45°) incidence (figure 2(d)), compared to thin films with either 2 μm thickness (same as NW length) or 167 nm thickness (same corresponding volume as the NWs). Furthermore, the simulated absorption photon density profiles (figures 2(e) and (f)) indeed indicate that tilting the sample causes increased absorption of high energy photons along the entire length of the NW [22], thus including the space-charge region, compared to just the tip. Under forward bias conditions and normal incidence, the space-charge region contracts towards the base of the NWs leading to a decreased relative PC contribution from the lower part of the NWs compared to the reverse-biased Schottky-like NW tip/ITO junction at the top. Upon tilting the sample, a regained relative PC contribution from the lower part of the NWs comprising the forward-biased p–n junction is observed both theoretically and experimentally (figures 2(c), (e) and (f)). Electroluminescence measurements (figure S4 in the online supplementary data) show no bias-dependent shift, as expected. The peak energy is in agreement with previous reports on InP NWs with mixed ZB/WZ crystal structure [12]. These observations also indicate the presence of a Schottky-like contact at the NW tip/ITO interface.

To verify the existence of such a contact resulting from an insufficient doping level in the top segment of the NWs, sample B (p^+–n^-–n^+) was subsequently fabricated where the indium flow rate was reduced resulting in a higher incorporation of Sn dopants in the top n^+-segment [19]. For sample B, no bias-dependent change in the spectral shape of the PC spectra was observed in the responsivity measurements (figure 3(a)). In addition, the peak with onset at about 3.0 eV, corresponding to interband excitation of ITO, was also suppressed in sample B compared to sample A (figure 2). Moreover, the PC obtained from lock-in chopper measurements did not show any change of sign (inset of figure 3(a)). The dark current in these devices was generally higher compared to sample A (figure 3(b)). The correlation between observed shoulders in the *I*–*V* at small forward biases and increased leakage current at reverse biases implies variations in processing of different sample batches.

The effect of doping in the absorption segment was compared by fabricating sample C (p^+–i–n^+) with no intentional doping in the absorption segment, (see Methods section for details). It was concluded that these samples displayed similar PC characteristics as sample B, with no high energy peaks at forward biases (figure S5 in the online supplementary data). One expected effect related to doping differences in the absorption segment is possible self-gating induced by the ITO/SiO_x/NW wrap-gate geometry (figure 1(a)). The radial electric field in such effective MOS-like structures could induce carrier depletion upon applying forward bias (positive potential applied to the NW core relative to the ITO acting as gate electrode) that would change the spatial distribution of the applied bias along the NW. Electrical simulations (see section 2.4 for details) using the expected doping profile for sample A (figures 4(a) and (b)) as well as sample B and C (not shown), however, reveal that the wrap gate could have a depletion effect only for small forward biases when the axial electric field is lower than 10^4 V cm^{-1}. At large forward bias, a significantly enhanced axial electric field in the upper part of the NW instead facilitates high-level carrier injection in the p–n junction. Such conditions could in fact also convert the upper part of the NW to a photoconductor and lead to positive (reversed) photocurrent generation (figures 4(c) and (d)).

The simulated *I*–*V* characteristics (figure 4(e)) are in good agreement with the measured results at small forward biases considering the mixed crystal structure in the NWs that could increase their effective ideality factor [12, 32]. However, at large forward bias the simulated current saturates at a much higher current level than any of the measured devices in this study. The most obvious current-limiting mechanism, often tacitly assumed in literature, is the presence of series resistance. Assuming a series resistance of 250 Ω in our case leads to a good match between measured and simulated

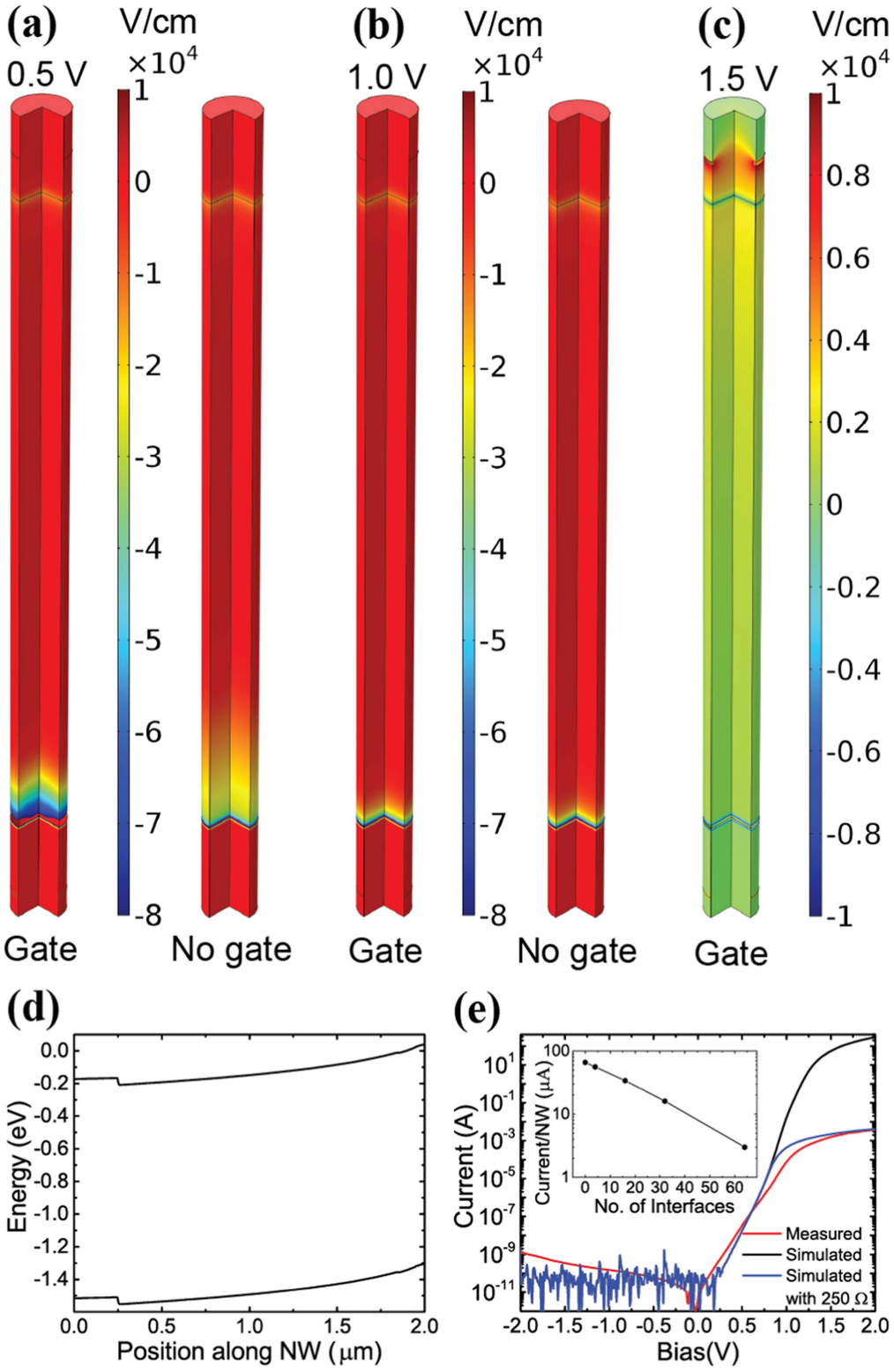

Figure 4. Simulated axial electric field with and without wrap-gate at (a) 0.5 V and (b) 1 V forward bias. (c) Axial electric field indicating high-level injection and (d) corresponding energy band diagram at 1.5 V forward bias. (e) Simulated *I–V* characteristics for a NW array with and without included 250 Ω series resistance compared to the measured results of sample A. Inset shows the current/NW at 2 V forward bias versus number of ZB/WZ interfaces.

current levels at high forward biases (figure 4(e)). The origin of such a high resistance could not be due to the sheet resistance of ITO (about 5 Ω) [33] or the ITO/NW contact resistance [30], although the exact morphology of the contact surface at the tip of the NWs is unknown. One plausible reason for current saturation in the measured samples could be excitation of electrons to the second conduction band (L-valley), induced by the high electric fields ($>10^4$ V cm^{-1},

figure 4(c)), where the drift velocity (effective mass) is lower (higher) than in the Γ-valley conduction band. This is the physical mechanism behind the well-known Gunn effect, typically observed in GaAs and InP bulk devices. Taking this saturation in drift velocity/mobility [28] into account (as mentioned in section 2.4), however, reduces the simulated currents by only a factor of 2. Another interesting current-limiting mechanism stems from scattering of carriers at ZB/WZ interfaces in the mixed crystal structure of the NWs [34], reducing the carrier mobility and thus the current (inset of figure 4(e)). Further in-depth studies are needed to fully understand the origin of the large series resistances typically observed for NW devices, which is beyond the scope of this work.

In conclusion, we have performed a study of the influence of doping profile and bias on the characteristics of photodetectors based on up to 4 million InP NWs connected in parallel in a vertical geometry. We report on bias-dependent tuning of the spectral shape of the responsivity in p^+–n^-–n InP NW devices attributed to a previously unobserved Schottky-like contact at the NW tip–ITO interface. Angular-dependent responsivity measurements compared with simulated absorption spectra in conjunction with electrical measurements substantiate this claim. The simulations of the electric field distribution demonstrate that possible self-gating effects induced by the effective wrap-gate geometry of NW array devices are typically small. The experimental *I*–*V* data saturates at a much lower current level than inferred from the modeling. Different physical mechanisms have been implemented in the models to account for the discrepancy, but the exact nature of the apparent high series resistance remains unknown. Possible effects of space-charge-limited current transport combined with carrier trapping in the complex polytype WZ/ZB mixed crystal landscape needs to be further investigated.

Acknowledgments

The authors thank Bernd Witzigmann from University of Kassel, Pyry Kivisaari and Yang Chen from Lund University for fruitful discussions on simulations. The authors also acknowledge financial support from NanoLund, the Ljungberg Foundation, the Carl Trygger Foundation, the Swedish Research Council, the Swedish National Board for Industrial and Technological Development, the Swedish Foundation for Strategic Research and the Swedish Energy Agency.

References

[1] Lu W and Lieber C M 2007 Nanoelectronics from the bottom up *Nat. Mater.* **6** 841–50
[2] Duan X, Huang Y, Cui Y, Wang J and Lieber C M 2001 Indium phosphide nanowires as building blocks for nanoscale electronic and optoelectronic devices *Nature* **409** 66–9
[3] Huang M H, Mao S, Feick H, Yan H, Wu Y, Kind H, Weber E, Russo R and Yang P 2001 Room-temperature ultraviolet nanowire nanolasers *Science* **292** 1897–9
[4] Wang J, Gudiksen M S, Duan X, Cui Y and Lieber C M 2001 Highly polarized photoluminescence and photodetection from single indium phosphide nanowires *Science* **293** 1455–7
[5] Pettersson H, Trägårdh J, Persson A I, Landin L, Hessman D and Samuelson L 2006 Infrared photodetectors in heterostructure nanowires *Nano Lett.* **6** 229–32
[6] Patolsky F and Lieber C M 2005 Nanowire nanosensors *Mat. Today* **8** 20–8
[7] LaPierre R R 2011 Theoretical conversion efficiency of a two-junction III–V nanowire on Si solar cell *J. Appl. Phys.* **110** 4310–5
[8] Tian B, Zheng X, Kempa T J, Fang Y, Yu N, Yu G, Huang J and Lieber C M 2007 Coaxial silicon nanowires as solar cells and nanoelectronic power sources *Nature* **449** 885–9
[9] Mariani G, Scofield A C, Hung C-H and Huffaker D L 2013 GaAs nanopillar-array solar cells employing in situ surface passivation *Nat. Commun.* **4** 1497
[10] Nowzari A, Heurlin M, Jain V, Storm K, Hosseinnia A, Anttu N, Borgström M T, Pettersson H and Samuelson L 2015 A comparative study of absorption in vertically and laterally oriented InP core–shell nanowire photovoltaic devices *Nano Lett.* **15** 1809–14
[11] Wallentin J, Anttu N, Asoli D, Huffman M, Åberg I, Magnusson M H, Siefer G, Fuss-Kailuweit P, Dimroth F, Witzigmann B, Xu H Q, Samuelson L, Deppert K and Borgström M T 2013 InP nanowire array solar cells achieving 13.8% efficiency by exceeding the ray optics limit *Science* **339** 1057–60
[12] Jain V, Nowzari A, Wallentin J, Borgström M, Messing M, Asoli D, Graczyk M, Witzigmann B, Capasso F, Samuelson L and Pettersson H 2014 Study of photocurrent generation in InP nanowire-based p^+–i–n^+ photodetectors *Nano Res.* **7** 1–9
[13] Mårtensson T, Carlberg P, Borgström M, Montelius L, Seifert W and Samuelson L 2004 Nanowire arrays defined by nanoimprint lithography *Nano Lett.* **4** 699–702
[14] Jam R J, Heurlin M, Jain V, Kvennefors A, Graczyk M, Maximov I, Borgström M T, Pettersson H and Samuelson L 2015 III–V nanowire synthesis by use of electrodeposited gold particles *Nano Lett.* **15** 134–8
[15] Wallentin J, Wickert P, Ek M, Gustafsson A, Wallenberg L R, Magnusson M H, Samuelson L, Deppert K and Borgström M T 2011 Degenerate p-doping of InP nanowires for large area tunnel diodes *Appl. Phys. Lett.* **99** 253105
[16] Borgström M T, Norberg E, Wickert P, Nilsson H A, Trägårdh J, Dick K A, Statkute G, Ramvall P, Deppert K and Samuelson L 2008 Precurson evaluation for in situ InP nanowire doping *Nanotechnology* **19** 5602
[17] Borgström M T, Wallentin J, Trägårdh J, Ramvall P, Ek M, Wallenberg L R, Samuelson L and Deppert K 2010 In-situ etching for total control over axial and radial nanowire growth *Nano Res.* **3** 264–70
[18] Wallentin J, Ek M, Wallenberg L R, Samuelson L and Borgström M T 2012 Electron trapping in InP nanowire FETs with stacking faults *Nano Lett.* **12** 151–5
[19] Lindelöw F, Heurlin M, Otnes G, Dagyte V, Hultin O, Storm K, Samuelson L and Borgström M T 2016 Doping evaluation of InP nanowires for tandem junction solar cells *Nanotechnology* **27** 065706
[20] Pettersson H, Zubritskaya I, Nghia N T, Wallentin J, Borgström M T, Storm K, Landin L, Wickert P, Capasso F and Samuelson L 2012 Electrical and optical properties of InP nanowire ensemble p^+–i–n^+ photodetectors *Nanotechnology* **23** 135201

[21] Borgström M T, Wallentin J, Heurlin M, Fält S, Wickert P, Leene J, Magnusson M H, Deppert K and Samuelson L 2011 Nanowires with promise for photovoltaics *IEEE J. Sel. Top. Quantum. Electron.* **17** 12

[22] Aghaeipour M, Pistol M E and Pettersson H 2017 Considering symmetry properties to gain broadband absorption in InP nanowires (in preparation)

[23] Rosenwaks Y, Shapira Y and Huppert D 1992 Picosecond time-resolved luminescence studies of surface and bulk recombination processes in InP *Phys. Rev.* B **45** 9108

[24] Joyce H J, Docherty C J, Gao Q, Tan H H, Jagadish C, Lloyd-Hughes J, Herz L M and Johnston M B 2013 Electronic properties of GaAs, InAs and InP nanowires studied by terahertz spectroscopy *Nanotechnology* **24** 214006

[25] Rosenwaks Y, Shapira Y and Huppert D 1991 Evidence for low intrinsic surface-recombination velocity on p-type InP *Phys. Rev.* B **44** 97–100

[26] Semyonov O, Subashiev A, Chen Z and Luryi S 2010 Radiation efficiency of heavily doped bulk n-InP semiconductor *J. Appl. Phys.* **108** 013101

[27] Levinshtein M, Rumyantsev S and Shur M 1996 *Handbook Series on Semiconductor Parameters* vol 1 (London: World Scientific)

[28] Mohammad S N, Bemis A V, Carters R L and Renbeck R B 1993 Temperature, electric field, and doping dependent mobilities of electrons and holes in semiconductors *Solid-State Electron.* **36** 1677–83

[29] Sotoodeh M, Khalid A H and Rezazadeh A A 2000 Empirical low-field mobility model for III–V compounds applicable in device simulation codes *J. Appl. Phys.* **87** 2890

[30] Luo J K and Thomas H 1993 The influence of indium tin oxide deposition on the transport properties at InP junctions *J. Electron. Mater.* **22** 1311–6

[31] Tsai M J, Fahrenbruch A L and Bube R H 1980 Sputtered oxide/indium phosphide junctions and indium phosphide surfaces *J. Appl. Phys.* **51** 2696–705

[32] Harada K, Werner A G, Pfeiffer M, Bloom C J, Elliott C M and Leo K 2005 Organic homojunction diodes with a high built-in potential: interpretation of the current–voltage characteristics by a generalized einstein relation *Phys. Rev. Lett.* **94** 6601–3

[33] Hao X T, Zhu F R, Ong K S and Tan L W 2005 Colour tunability of polymeric light-emitting diodes with top emission architecture *Semicond. Sci. Technol.* **21** 19–24

[34] Thelander C, Caroff P, Plissard S, Dey A W and Dick K A 2011 Effects of crystal phase mixing on the electrical properties of InAs nanowires *Nano Lett.* **11** 2424–9